Materials Advances

ROYAL SOCIETY OF CHEMISTRY

PAPER

View Article Online
View Journal | View Issue

Cite this: *Mater. Adv.*, 2026, 7, 2652

Analysis of the magnetic dipolar nonradiative decay of the $^5D_1$ level of Eu^{3+} in single-crystalline huntite-type $REAl_3(BO_3)_4$:Eu^{3+} (RE = Y, Gd, Lu)†

Tom Förster, [a] Leonardo Ceccon, [b] Benedikt Bendel, [a] Marco Bettinelli, [b] Fabio Piccinelli *[b] and Markus Suta *[a]

The intraconfigurational $4f^6 \leftrightarrow 4f^6$ transitions of Eu^{3+} provide sensitive insights into local symmetry and ligand fields, making Eu^{3+} a versatile probe ion for structural elucidation and temperature-dependent optics. In particular, the dynamics of the $^5D_1$ level are of central importance for applications in ratiometric luminescence thermometry but are strongly influenced by the phonon energy of the host compound, selection rules and the average Eu–ligand distance. In Eu^{3+}-activated huntite-type borates $REAl_3(BO_3)_4$ (RE = Y, Gd, Lu), there is an almost trigonal prismatic coordination with a local D_3 symmetry of the RE^{3+} ion, whose subtle distortions vary systematically from RE = Gd to RE = Y to RE = Lu. These structural changes are reflected in a slight elongation of the $^5D_0$ decay time and a decreasing asymmetry ratio R_2, indicating a reduced induced electric–dipole component according to Judd–Ofelt theory. Temperature-dependent photoluminescence and time-resolved measurements determine the intrinsic nonradiative coupling rate between the $^5D_1$ and $^5D_0$ levels to be $k_{nr}(0) \approx 55\ ms^{-1}$. As expected, this increases with a shorter Eu–O bond lengths, but in $GdAl_3(BO_3)_4$, it shows an additional contribution that cannot be explained structurally and is attributed to a local acceleration effect caused by the paramagnetism of the surrounding Gd^{3+} ions. The temperature dependence of the $^5D_0$ decay time also reveals a thermal coupling of the excited states and a high-temperature-induced quenching *via* the $Eu^{3+} \leftarrow O^{2-}$ ligand-to-metal charge transfer (LMCT) state. These results provide a comprehensive understanding of the excited state dynamics of Eu^{3+} in huntite-type borate and, at the same time, illustrate the potential and limitations of these host lattices for Eu^{3+}-based luminescence thermometry.

Received 17th December 2025,
Accepted 21st January 2026

DOI: 10.1039/d5ma01480h

rsc.li/materials-advances

Introduction

Frequently used luminescent solid-state materials are based on the targeted activation of host compounds containing lanthanoid ions. A particularly popular candidate in this regard is Eu, which is used in both its divalent and trivalent oxidation state. While divalent europium (Eu^{2+}) mainly shows broad-band luminescence based on an electric dipole-allowed $4f^65d^1 \rightarrow 4f^7$ transition that can be specifically varied in energy by choosing the host compound,[1–9] Eu^{3+} is much more prominent for its narrow-line luminescence related to intraconfigurational $4f^6 \leftrightarrow 4f^6$ transitions.[10–16] Eu^{3+} primarily exhibits luminescence from its lowest excited $^5D_0$ level to the lower-energy ^7F_J (J = 0–4) levels in the red spectral range[17] and finds numerous applications in bioimaging[18–20] and solid-state lighting.[21–24]

The excited $^5D_0$ level and the ground level $^7F_0$ of Eu^{3+} are both singly degenerate and thus, will not be split any further in a crystal field. As a consequence, the number and relative intensities of observed lines in the absorption and luminescence spectra of Eu^{3+}-activated compounds can give insights about the local symmetry of the sites that the Eu^{3+} ions occupy.[24–28] Accordingly, Eu^{3+} can be used for the spectral determination of site symmetry to characterize the environment.[27–32]

Among the intraconfigurational $4f^6 \leftrightarrow 4f^6$ transitions of the Eu^{3+} ion, the $^5D_0 \rightarrow {}^7F_1$ transition and the $^5D_0 \rightarrow {}^7F_2$ transition are particularly important. The former is a pure magnetic dipolar transition[33–35] and its intensity is largely independent of local symmetry, depending mainly on the refractive index.[36] The latter, on the other hand, is an induced electric dipolar transition,[34,35,37,38] according to the Judd–Ofelt theoretical framework,[39,40] and its intensity can be tuned by an appropriate choice of the ligand field environment. The intensity ratio of these two transitions (called asymmetry ratio R_2) is often used to make statements about the

[a] *Inorganic Photoactive Materials, Institute of Inorganic Chemistry and Structural Chemistry II, Heinrich Heine University Düsseldorf, Universitätsstraße 1, 40225 Düsseldorf, Germany. E-mail: markus.suta_at_hhu.de*
[b] *Luminescent Materials Laboratory, Department of Biotechnology, University of Verona and INSTM, UdR Verona, Strada Le Grazie 15, Verona, 37134, Italy. E-mail: fabio.piccinelli_at_univr.it*

† Dedicated to our friend Luís Carlos on the occasion of his 60th birthday.

local symmetry of the environment and can be even photonically controlled on the nanoscale.[26,41] Recently, the impact of the polarizability of the ligating atoms around Eu^{3+} on the R_2 values, has been also discussed.[42]

Furthermore, luminescence from the higher-energy $^5D_1$ level (Fig. 1) can be observed, making Eu^{3+} in principle suited for ratiometric luminescence thermometry as well.[44,45] It turns out that the energy gap of $\Delta E \approx 1750\ cm^{-1}$ between the excited $^5D_1$ and $^5D_0$ level is generally useful for high temperatures. In addition to the selected host compound based on their phonon energies,[17,46] also selection rules[47] and the average Eu–ligand distance may affect the nonradiative decay of the $^5D_1$ level thus having an impact on performance of an Eu^{3+}-based luminescence thermometer.[17,46,48]

Rare earth aluminum borates in the huntite-type structure represent an interesting class of host compounds for the luminescence of trivalent lanthanoid ions.[49,50] In particular, Yb^{3+}- and Nd^{3+}-activated $REAl_3(BO_3)_4$ (RE = Y, Gd) have attractive properties for use in solid-state lasers.[51–55] The optical spectroscopy of huntite borate crystals activated with the Eu^{3+} ion has been investigated in the past by Görller-Walrand *et al.*[56,57] and by Kellendonk and Blasse.[58] In this work, we analyze the excited state dynamics of the $^5D_1$ level of Eu^{3+} in the isotypically crystallizing huntite-type series $REAl_3(BO_3)_4$ (RE = Y, Gd, Lu). We will elaborate on the impact of the varying average Eu–O bond lengths. In addition, a possibly accelerating influence of the paramagnetic nature of Gd^{3+} compared to the other two diamagnetic rare-earth ions on the expectedly magnetic dipolar $^5D_1 \leftrightarrow {}^5D_0$ transition will be investigated.

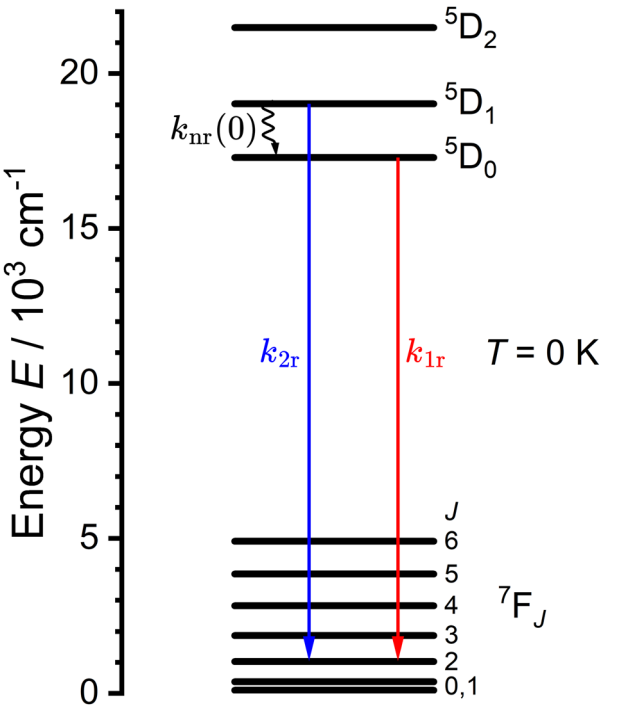

Fig. 1 Energy level diagram of Eu^{3+}. The radiative (blue) and nonradiative decay (black) of the $^5D_1$ level and the radiative decay of the $^5D_0$ (red) level are shown for an idealized temperature of T = 0 K. Energies were taken from the data published by Dieke *et al.*[43]

Synthesis and methods

The synthesis of $REAl_3(BO_3)_4$ (RE = Y, Gd, Lu) single crystals and the instrumentation used for this study are detailed in the SI.

Results and discussion

Structural analysis

The XRD analysis reveals that the Eu^{3+}-activated $REAl_3(BO_3)_4$ (RE = Y, Gd, Lu) compounds crystallize in a trigonal crystal system with the space group $R32$ (no. 155) in a huntite-type structure that can be considered as a filled version of the calcite ($CaCO_3$) structure type. The obtained XRD patterns indicate phase purity of the phosphors (Fig. S1). In line with the different ionic radii of the considered rare-earth ions, reflections show a consistently decreasing lattice parameters from Gd^{3+} over Y^{3+} to Lu^{3+} (see Table S1). As expected, the RE–O bond lengths also decrease in this series of rare-earth ions (Table S1).

The crystal structure of $REAl_3(BO_3)_4$ (RE = Y, Gd, Lu) is depicted in Fig. 2(a).[59] The RE^{3+} ions occupy six-fold coordinated sites with nearly ideal trigonal prismatic coordination geometry and a local D_3 point symmetry (see Fig. 2(b)). The RE^{3+} cations are shielded from each other by trigonal-planar $[BO_3]^{3-}$ units, resulting in large distances between the nearest RE^{3+} sites ($\approx$5.9 Å), which limits possible decay pathways such as concentration quenching, whilst allowing the detailed study of energy transfer and migration processes when suitable cations are present in the structure.[60–62]

Photoluminescence of Eu^{3+} in $REAl_3(BO_3)_4$ (RE = Y, Gd, Lu)

The photoluminescence excitation and emission spectra of Eu^{3+} in single-crystalline $REAl_3(BO_3)_4$ (RE = Y, Gd, Lu) at 81 K are depicted in Fig. 3. The excitation spectra recorded upon monitoring the $^5D_0 \rightarrow {}^7F_2$ transition of Eu^{3+} at around 613 nm reveal narrow-line transitions to the $^5D_0$ (580 nm) and higher $4f^6$ levels such as the $^5D_1$ (525 nm), $^5D_2$ (460 nm), $^5L_6$ (395 nm) and $^5D_4$ level (360 nm). Additionally, a broad excitation band in the UV range (at around 260 nm) is observed, which can be attributed to the $Eu^{3+} \leftarrow O^{2-}$ ligand-to-metal charge transfer (LMCT) state and is commonly observed in complex oxides.[11,60,63–67] In $GdAl_3(BO_3)_4$:1% Eu^{3+}, additional narrow-line transitions in the UV range at around 310 nm, 300 nm and 270 nm are observed, which are attributed to $4f^7 \leftrightarrow 4f^7$ transitions of Gd^{3+}.[47,68,69]

The emission spectra show narrow bands in the orange and red range, which are typical for luminescence from the $^5D_0$ level to the lower energetic $^7F_1$, $^7F_2$, $^7F_3$ and $^7F_4$ levels. The number of emission bands (2 for the $^5D_0 \rightarrow {}^7F_1$, 2 for the $^5D_0 \rightarrow {}^7F_2$, 4 for the $^5D_0 \rightarrow {}^7F_3$, and 4 for the $^5D_0 \rightarrow {}^7F_4$ transition) indicates a D_3 point symmetry for Eu^{3+},[25] in excellent agreement with the local structure of the distorted $[REO_6]^{9-}$ (RE = Y, Gd, Lu) trigonal prisms (Fig. 2). In addition to the emission from the $^5D_0$ level, also weak emission from the higher-energetic $^5D_1$ level into the $^7F_0$, $^7F_1$, and $^7F_2$ levels (520–570 nm) can be detected. The comparably weak emission from the $^5D_1$ level can be explained by rapid multiphonon relaxation due to the high cut-off phonon

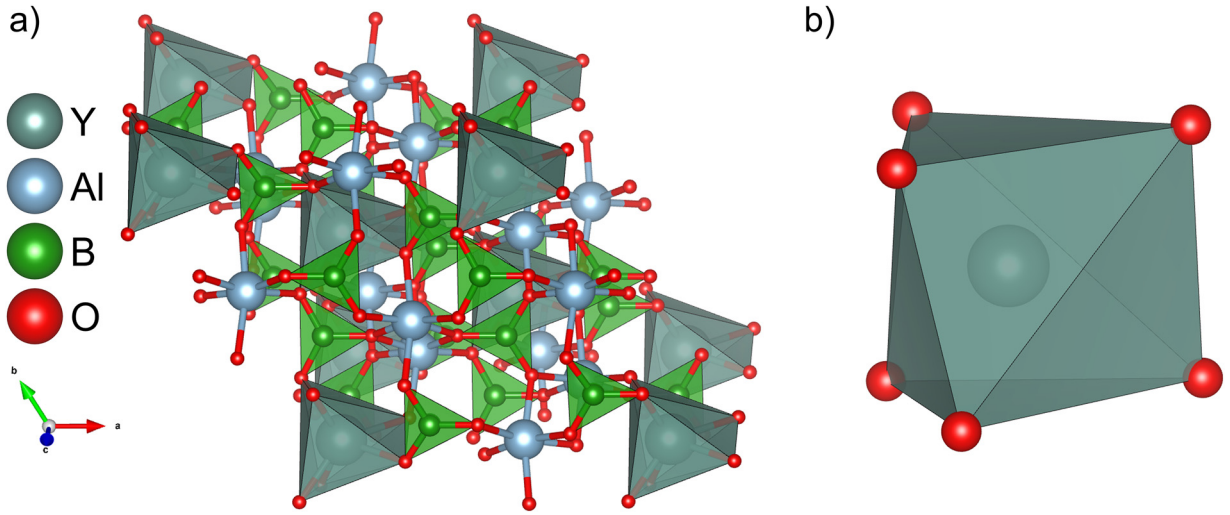

Fig. 2 (a) Crystal structure of $YAl_3(BO_3)_4$ (ICSD: 20223) visualized by VESTA. (b) Coordination of the Y site.

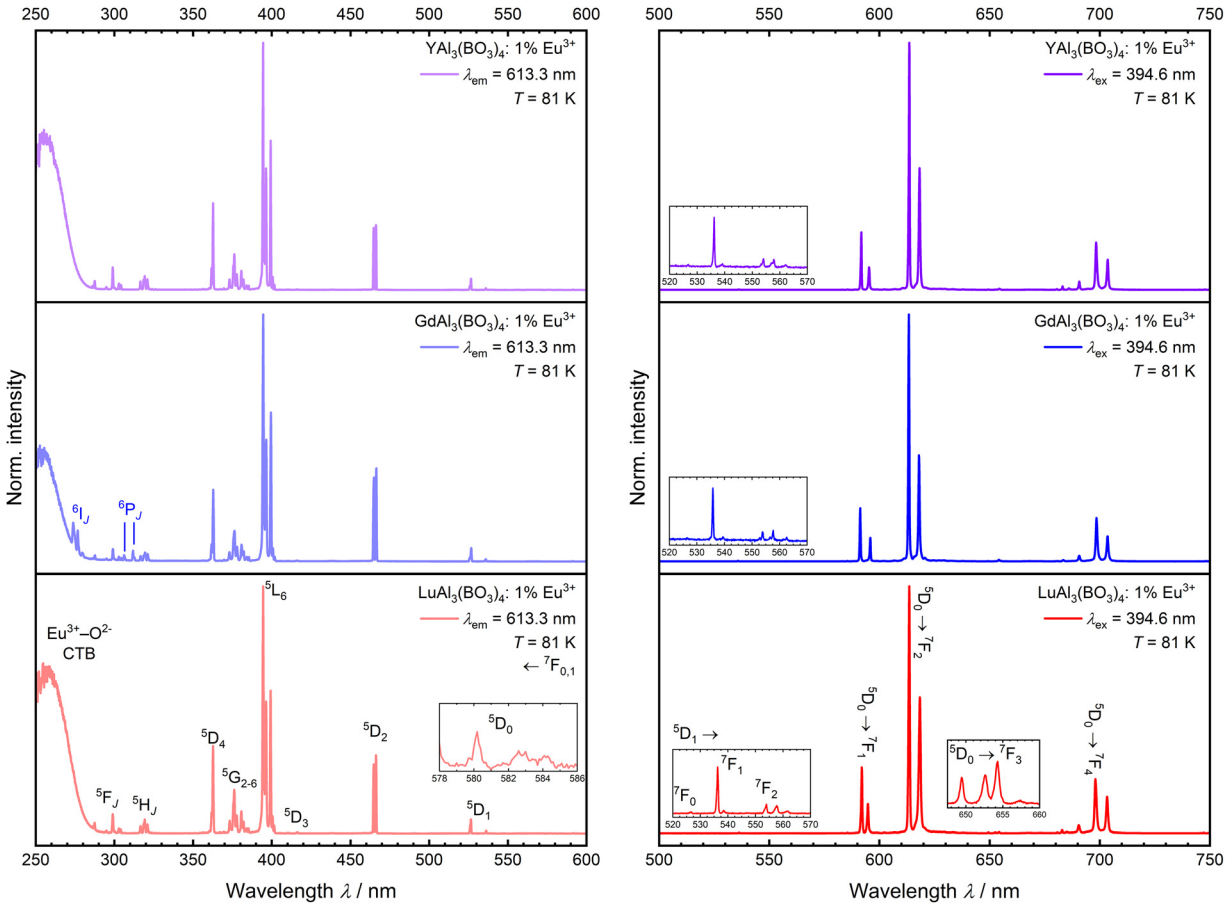

Fig. 3 Normalized photoluminescence excitation (left) and emission spectra (right) of $REAl_3(BO_3)_4$:1% Eu^{3+} (RE = Y, Gd, Lu) at 81 K. For excitation spectra, the emission from the $^5D_0 \rightarrow {}^7F_2$ transition was monitored. Emission spectra were recorded upon excitation into the $^5L_6$ level. The assignment of Eu^{3+}-based transitions is exemplarily depicted for the case of $LuAl_3(BO_3)_4$:1% Eu^{3+}.

energy in $REAl_3(BO_3)_4$ ($\hbar\omega_{cut} \approx 1400\ cm^{-1}$).[70] The excitation spectra reveal an energy gap of $\Delta E \approx 1750\ cm^{-1}$ between the $^5D_1$ and $^5D_0$ level of Eu^{3+} in these compounds (see SI), which is in agreement with other works.[44,48,71–73]

Fig. 4 depicts the measured decay curves of the $^5D_1$- and $^5D_0$-based emission of Eu^{3+} in $REAl_3(BO_3)_4$ (RE = Y, Gd, Lu) at 81 K, respectively. The luminescence intensity stemming from both excited levels in the 1 mol%-activated borates show single

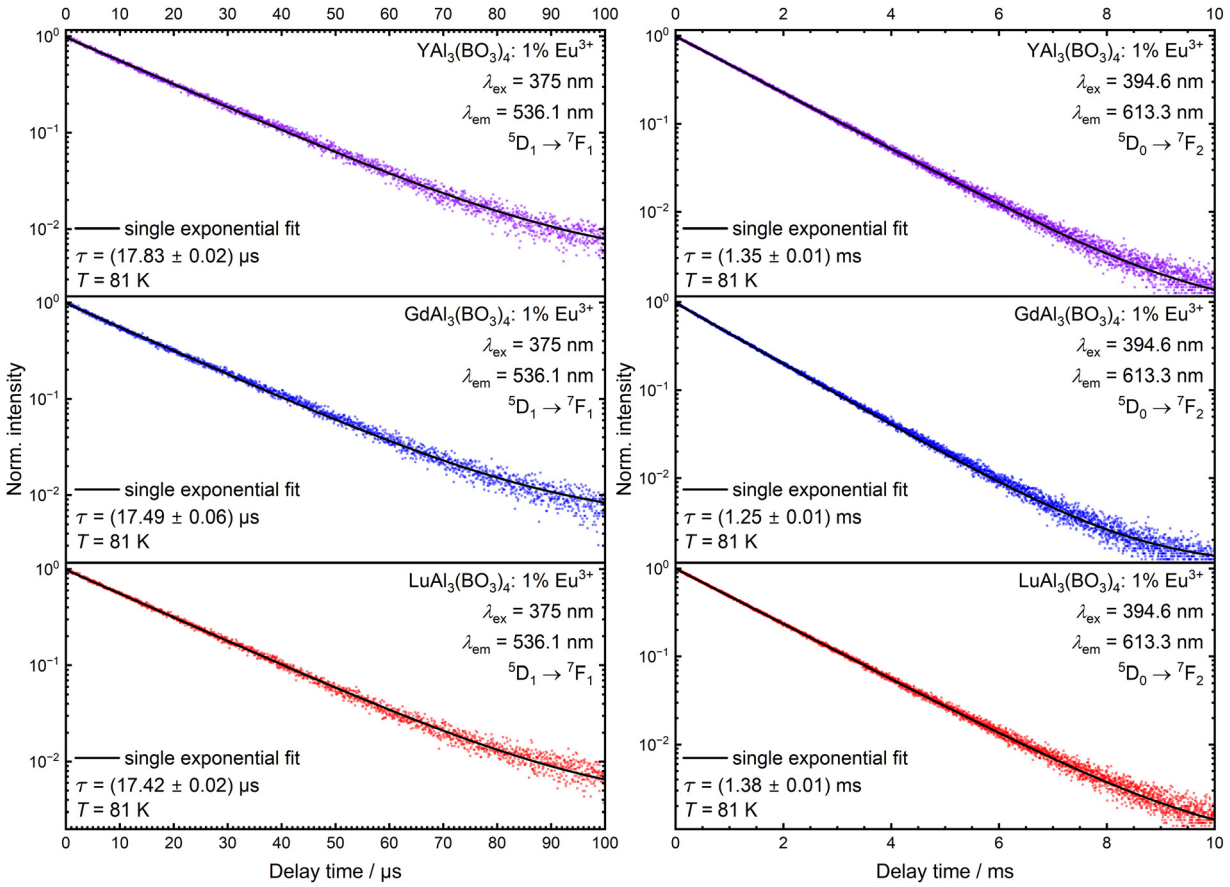

Fig. 4 Photoluminescence decay curves with single exponential fits (black) of the $^5D_1$-based (left, μs range) and the $^5D_0$-based emission (right, ms range) of $REAl_3(BO_3)_4$:1% Eu^{3+} (RE = Y, Gd, Lu) at 81 K.

exponential decay clearly justifying the assumption of negligible cross-relaxation or additional interaction processes among the Eu^{3+} ions at that temperature, which is consistent with the structure and the associated high RE–RE distances of more than 5 Å. The decays remain single exponential even at temperatures up to 823 K (see Fig. S4 in the SI). Cross-relaxation involving the $^5D_1$ level is often manifested by a fast component at short delay times in the decay curve, especially at higher temperatures.[71,74–76]

Due to the high energy gap between the $^5D_0$ and the $^7F_6$ level (Fig. 1), the decay of the $^5D_0$ level can be assumed to be purely radiative. The $^5D_0$ level of Eu^{3+} in $REAl_3(BO_3)_4$ (RE = Y, Gd, Lu) can be characterized by a decay time of just above 1 ms (see Table 1) at 81 K, which is consistent with Eu^{3+} in other host compounds.[11,65,77–79] The measured decay time of the $^5D_0$ level in $REAl_3(BO_3)_4$:1% Eu^{3+} shows a measurable increase from RE = Gd over RE = Y to RE = Lu. Inspection of the local coordination geometry of the $[REO_6]^{9-}$ entities (see Fig. 5) according to single-crystal (RE = Gd, Y) or Rietveld refined (RE = Lu; Fig. S1) structural data reveals that the angle between the two planes defined by $O3^v$–$O3^i$–$O3^{iv}$ and $O3^v$–$O3^i$–$O3^{iii}$ (Table 2) decreases from Gd over Y to Lu (34.5° → 30.0° → 26.1°), suggesting a gradual evolution of the (distorted) trigonal prism geometry towards a (distorted) octahedral one (from Gd to Lu). According to Judd–Ofelt theory,[39,40] a stronger induced electric dipolar character of the radiative transitions of Eu^{3+} should be detectable in non-centrosymmetric site symmetries (represented by the trigonal prismatic coordination geometry), inducing a decrease in the $^5D_0$ observed lifetime. Also, this interpretation goes in line with the decreasing splitting between the two Stark components of the $^7F_1$ level (see $^5D_0 \rightarrow {}^7F_1$ transition in the emission spectra of Fig. 3 or $^5D_1 \leftarrow {}^7F_0$ transition in the excitation spectra of Fig. S3 in the SI), which gradually decreases along that series of rare earth ions, as a $|J=1\rangle$ level retains its triple degeneracy in the limiting case of octahedral symmetry. Additional confirmation is gained from the asymmetry ratio R_2, which can be derived from the emission spectrum as[26,42]

$$R_2 = \frac{I_{^5D_0 \rightarrow {}^7F_2}}{I_{^5D_0 \rightarrow {}^7F_1}} \quad (1)$$

Table 1 Measured decay time τ of the $^5D_0$ level, the asymmetry ratio R_2 according to eqn (1) and the intensity ratio of the $^5D_2 \leftarrow {}^7F_0$ and $^5D_1 \leftarrow {}^7F_0$ excitation transitions (Fig. 3) of $REAl_3(BO_3)_4$:1% Eu^{3+} (RE = Y, Gd, Lu) at T = 81 K

Compound	$\tau(^5D_0)$/ms	R_2	$I(^5D_2/^5D_1)$
$YAl_3(BO_3)_4$:1% Eu^{3+}	1.35 ± 0.01	5.568 ± 0.003	8.872 ± 0.001
$GdAl_3(BO_3)_4$:1% Eu^{3+}	1.25 ± 0.01	5.644 ± 0.003	10.885 ± 0.001
$LuAl_3(BO_3)_4$:1% Eu^{3+}	1.38 ± 0.01	5.266 ± 0.002	8.807 ± 0.001

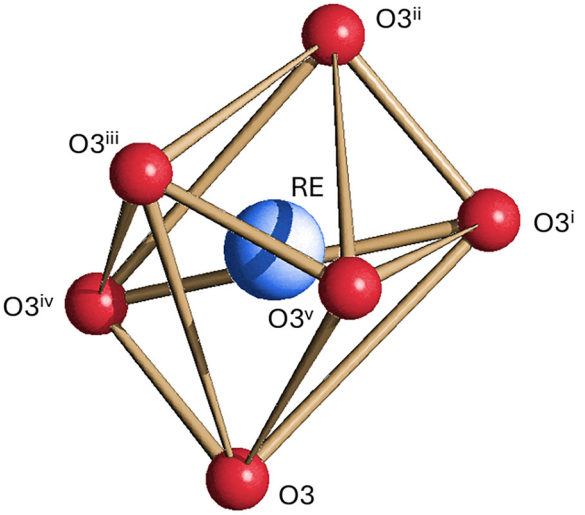

Fig. 5 Coordination environment of the RE^{3+} ion in $REAl_3(BO_3)_4$ (RE = Y, Gd, Lu). Relevant bond lengths and angles are reported in the SI (Fig. S2 and Table S2).

Table 2 Definition of a distorted octahedral surrounding by the angle between the two planes defined by $O3^v$–$O3^i$–$O3^{iv}$ and $O3^v$–$O3^i$–$O3^{iii}$ according to Fig. 5 in $REAl_3(BO_3)_4$ (RE = Y, Gd, Lu). Relevant bond distances and angles are reported in the SI (Fig. S2 and Table S2)

Compound	Angle/° between the planes $O3^v$–$O3^i$–$O3^{iv}$ and $O3^v$–$O3^i$–$O3^{iii}$
$GdAl_3(BO_3)_4$	34.5(1)
$YAl_3(BO_3)_4$	30.0(1)
$LuAl_3(BO_3)_4$:1% Eu^{3+}	26.1(1)
Ideal octahedron	0

and decreases from RE = Gd over RE = Y to RE = Lu (see Table 1) in $REAl_3(BO_3)_4$:1% Eu^{3+} thus suggesting a more dominant magnetic dipolar nature of the $4f^6 \leftrightarrow 4f^6$ transitions of Eu^{3+} along this series.

Next to the established asymmetry ratio R_2, the intensity ratio of the excitation transitions $^5D_2 \leftarrow {}^7F_0$ and $^5D_1 \leftarrow {}^7F_0$ may also give additional independent confirmation on this hypothesis (see Fig. 3), as the former of the two transitions also has induced electric dipolar character according to Judd–Ofelt theory.[39,40] It should be noted, however, that line strengths in photoluminescence excitation spectra are only a good estimate for oscillator strengths (normally only accessible from absorption spectra) in the limit of low optical densities.[80] Given the low absorbance of $4f^6 \leftarrow 4f^6$ transitions as well as the low activator fraction of only 1 mol% of Eu^{3+}, this seems to be a reasonable approximation. In fact, the intensity ratio of the indicated excitation transitions in $REAl_3(BO_3)_4$:1% Eu^{3+} does follow the same trend as R_2 (see Table 1). This parallel course of the two independent ratios thus strongly indicates the validity of the proposed structure–property correlation.

Excited-state dynamics of the $^5D_1$ and $^5D_0$ levels of Eu^{3+}

In contrast to the $^5D_0$ level, the $^5D_1$ level in this set of compounds decays within around 17 μs (see Fig. 4). This much faster decay can be attributed to the additional contribution of multiphonon relaxation from the $^5D_1$ into the $^5D_0$ level. In the following, the small differences in the intrinsic nonradiative coupling rate between the $^5D_1$ and $^5D_0$ level of Eu^{3+} in $REAl_3(BO_3)_4$:1% Eu^{3+} (RE = Y, Gd, Lu) will be analyzed in more detail. For that purpose, temperature-dependent luminescence spectra were recorded for all three Eu^{3+}-activated borates upon excitation into the $^5L_6$ level at 395 nm (Fig. 6). The emission intensity of the $^5D_1$-based transitions increases with rising temperature, which suggests a gradual thermal population of the $^5D_1$ level. The temperature-dependent luminescence intensity ratio (LIR) can give valuable insights here and tested against a temperature-dependent steady-state model. As the energy gap between the $^5D_1$ and the $^5D_0$ levels ($\Delta E \approx 1750\ cm^{-1}$) cannot be bridged just by one cut-off phonon mode, but will also need a participation of at least one other (optical) phonon mode, the steady-state LIR can be modeled using the following equation[17]

$$\frac{I_2}{I_1} = C \times \frac{\alpha k_{1r} + g_2 k_{nr}(0)\langle n_1\rangle\langle n_2\rangle^{p_2}}{k_{2r}(1-\alpha) + g_1 k_{nr}(0)(1+\langle n_1\rangle)(1+\langle n_2\rangle)^{p_2}} \quad (2)$$

with I_j (j = 1, 2) as the intensities of the emission from the lower ($^5D_0 \equiv |1\rangle$) and higher energetic ($^5D_1 \equiv |2\rangle$) excited levels with degeneracies $g_1 = 1$ and $g_2 = 3$, respectively, C as the pre-factor, which is the ratio between the Einstein coefficients A_{j0} for spontaneous emission from the two levels, k_{1r} and k_{2r} as total radiative rates of the respective levels, α as a feeding factor, which describes the fraction of population from the pumped excited auxiliary level (here: $^5L_6$) into the higher excited level $^5D_1$, $k_{nr}(0)$ as the intrinsicnonradiative coupling rate between the two excited levels, and $\langle n_k\rangle$ (k = 1, 2) as the thermal phonon occupation factors of a regarded mode k with energy $\hbar\omega_2$,

$$\langle n_k\rangle = \frac{1}{\exp\left(\frac{\hbar\omega_k}{k_B T}\right) - 1} \quad (3)$$

with k_B as the Boltzmann constant and T as the absolute temperature. The phonon energies are constrained by the restriction $\Delta E_{21} = \sum_k \hbar\omega_k = \hbar\omega_1 + p_2\hbar\omega_2$. It can be shown that the generalized model (1) evolves into a classic Boltzmann distribution if the terms connected with $k_{nr}(0)$ are much larger than those containing the radiative rates, which is the case at sufficiently high temperatures.[46]

At very low temperatures, the LIR remains constant indicating that the two excited $^5D_1$ and $^5D_0$ levels of Eu^{3+} are decoupled in that regime (Fig. 6). Once low energetic phonon modes can be thermally activated, the LIR shows a slight drop as a consequence of thermally stimulated nonradiative relaxation of the $^5D_1$ level in favor of an accelerated population of the $^5D_0$ level. If the overall nonradiative absorption transition from the $^5D_0$ to the $^5D_1$ level can compete with the radiative decay k_{1r} of the $^5D_0$ level, the LIR rises again and the two excited levels get into thermal equilibrium, which manifests in a Boltzmann behavior of the temperature-dependent LIR.[17] For the investigated borates $REAl_3(BO_3)_4$:1% Eu^{3+} (RE = Y, Gd, Lu), the radiative rate of the $^5D_0$ level k_{1r} was fixed to the experimentally obtained values (Fig. 4), and the feeding factor was set to α = 1,

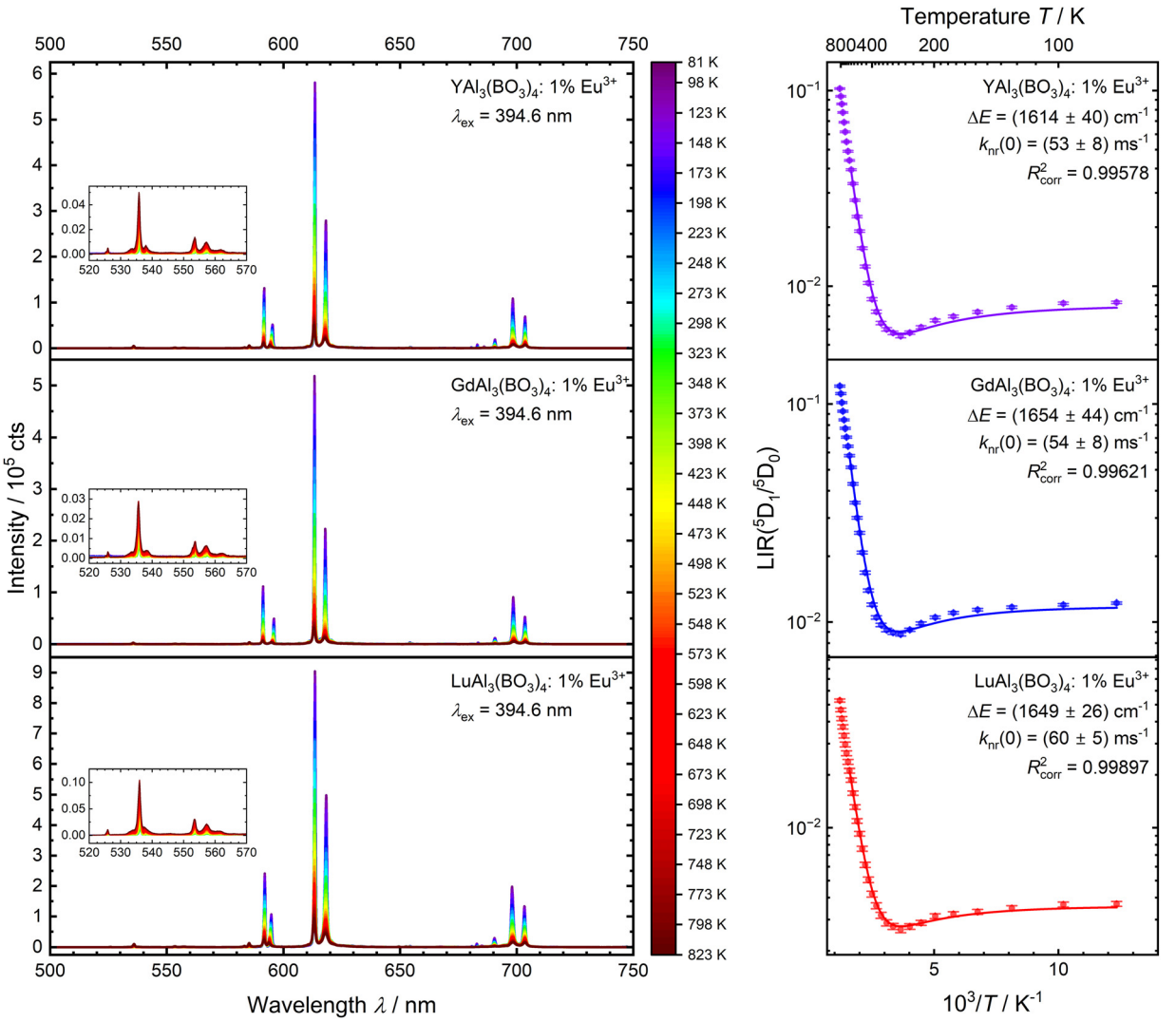

Fig. 6 Temperature-dependent emission spectra of $REAl_3(BO_3)_4$:1% Eu^{3+} (RE = Y, Gd, Lu) after excitation into the $^5L_6$ level (left) and the resulting luminescence intensity ratio with fit according to eqn (2) (right). The $^5D_1$-based emission is depicted in the inset.

as no emission from higher energetic levels is observed in the luminescence spectra at 81 K (Fig. 3). The cut-off phonon energy was set to $\hbar\omega_{max}$ = 1400 cm^{-1} (ref. 70) and the number of additional phonons to p_2 = 1.

The model can describe the LIR very accurately and the fit yields physically reasonable results (Fig. 6). The obtained energy gap is in the range of $\Delta E \approx 1650$ cm^{-1} and is generally fits in quite good agreement with the effective gap extracted from the excitation spectra ($\approx$ 1750 cm^{-1}) (see SI). The logarithmic LIR changes its slope at high temperatures ($T > 650$ K), which is unusual for classic Boltzmann thermalization (see Fig. 6). We attribute this behavior to the involvement of the $Eu^{3+} \leftarrow O^{2-}$ LMCT state (see Fig. 3) that can act as a crossover quenching pathway for the Eu^{3+} luminescence.[17,81,82] This hypothesis is confirmed by the observable decrease of the decay time of the $^5D_0$ level above 650 K (see Fig. 8), which will be discussed in more detail below. The influence of the LMCT state limits the applicability of the fitting model (1) at high temperatures. Thus, the limited temperature range for Boltzmann behavior of the LIR may also be the reason why the extracted energy gap from the fit does not fully match the spectroscopically extracted one from the excitation spectra at 81 K (see SI).

The intrinsic nonradiative rate according to the fits to eqn (2) are very similar and all in the range of $k_{nr}(0) \approx 55$ ms^{-1}, which is generally plausible given the fact that the cut-off (optical) phonons are typically dominated by localized ligand-related vibrations. This places the rate within the expected range for host compounds with high cut-off phonon energies, such as aragonite-type $LaBO_3$ ($k_{nr}(0)$ = 74 ms^{-1}).[17]

The range of application for a luminescent thermometer is largely defined by the so-called onset temperature T_{onset}, at which two thermally coupled levels are in thermal equilibrium.[46] This equilibrium is defined by the kinetic condition of competitve nonradiative multiphonon absorption compared to the radiative rate of the lower energy state, which equals $k_{1r} = k_{nr}(0) \times g_2 \times \langle n_1 \rangle \times \langle n_2 \rangle^{p_2}$ for our Eu^{3+}-activated borates.[17] The solution to this condition is numerical and yields onset temperatures in the

range of $T_{onset} \approx 400$ K. This means that the onset temperatures for $REAl_3(BO_3)_4$:1% Eu^{3+} (RE = Y, Gd, Lu) are in a similar range to other Eu^{3+}-based phosphors with high phonon energies, like $LaBO_3$:0.5% Eu^{3+} (T_{onset} = 402 K)[17] and $LaPO_4$:0.5% Eu^{3+} (T_{onset} = 396 K).[17] It should be noted that the onset temperatures heavily depend on the phonon energy $\hbar\omega_2$ obtained from the fit to eqn (2) and the associated thermal phonon occupation factor $\langle n_2 \rangle$. This can result in significant differences. Thus, the onset temperature can only serve as an estimate to judge the performance of a luminescent thermometer.

A comparison of the individual intrinsic nonradiative rates in $REAl_3(BO_3)_4$ (RE = Y, Gd, Lu) shows no discernible trend (Table 3). It has been demonstrated by Ermolaev and Sveshnikova in the case of molecular emitters[83] as well by some of us in microcrystalline β-$NaREF_4$:0.5% Eu^{3+} (RE = La, Y, Lu)[17] that the intrinsic nonradiative rate of Eu^{3+} should decrease with increasing average RE–ligand distance as vibrational coupling becomes weaker then.[17] The estimated values for the nonradiative transition rates $k_{nr}(0)$ according to the fits of the temperature-dependent LIR between the $^5D_1$ and $^5D_0$-based emission to eqn (2) does not readily allow such conclusions based on the large error margins of the values. Out of that reason, we performed time-resolved measurements of the luminescence decay of the $^5D_1$-based emission at 81 K to enhance the precision of the found values and motivate the validity of the order of magnitude estimated from the fit to eqn (2). At that temperature, nonradiative absorption from the $^5D_0$ to the $^5D_1$ level is negligible and thus, the total decay rate k_2 of the $^5D_1$ level contains the radiative contribution k_{2r} as well as the intrinsic nonradiative relaxation contribution $k_{nr}(0)$ to the $^5D_0$ level[46]

$$k_2 = k_{2r} + g_1 \times k_{nr}(0) \quad (4)$$

Upon selective pumping of the excited $^5D_1$ level (λ_{ex} = 525 nm) of Eu^{3+} in the huntite-type borates under investigation at a sufficiently low temperature (in order to prevent any thermalization among the excited levels), the ratio of the radiative rate of the $^5D_1$ level to the nonradiative rate can then be derived from the ratio of the luminescence intensities of the transitions stemming from the $^5D_1$ ($^5D_1 \equiv |2\rangle$) and $^5D_0$ ($^5D_0 \equiv |1\rangle$) level, respectively,[46]

$$\frac{I_2}{I_1} = \frac{k_{2r}}{g_1 \times k_{nr}(0)} \quad (5)$$

By rearranging eqn (4) as a function of k_{2r}, substituting it into eqn (5), and transforming it to a function of $k_{nr}(0)$, we thus obtain

$$k_{nr}(0) = \frac{k_2}{g_1} \times \left(\frac{I_2}{I_1} + 1\right)^{-1} \quad (6)$$

eqn (6) relates $k_{nr}(0)$ to the total cumulative intensity of all radiative transitions from a given level $|i\rangle$. In practice, often only one particular transition with intensity I_{ij} is considered. This can be accounted for by inclusion of the branching ratio $\beta_{i\to J}$ of a given transition from the respective level $|i\rangle$ into a lower energetic level $|J\rangle$, resulting in ref. 46

$$k_{nr}(0) = \frac{k_2}{g_1} \times \left(\frac{\beta_{1\to J} \times I_{2J}}{\beta_{2\to J} \times I_{1J}} + 1\right)^{-1} \quad (7)$$

with[26]

$$\beta_{i\to J} = \frac{I_{iJ}}{\sum_J I_{iJ}} \quad (8)$$

The emission spectra upon selective excitation into the $^5D_1$ level are depicted in Fig. 7. As for the spectra measured upon excitation into the $^5L_6$ level (Fig. 3), the Eu^{3+}-related emission from the $^5D_0$ level dominates, which indicates a comparably fast nonradiative decay from the $^5D_1$ level to the $^5D_0$ level compared to its radiative rate. Nevertheless, weak emission in the range of 550–565 nm can be observed, which is attributed to the $^5D_1 \rightarrow {}^7F_2$ transition. Consequently, the nonradiative rate can be calculated if the branching ratio for the $^5D_1 \rightarrow {}^7F_2$ transition is known. The branching ratios for the $^5D_1 \rightarrow {}^7F_2$ ($\beta_{1\to 2}$) and the $^5D_0 \rightarrow {}^7F_2$ ($\beta_{0\to 2}$) transitions were calculated from the emission spectra shown in Fig. 3 and are listed in Table 3. The intensities were determined from the emission spectra in Fig. 7c.

The nonradiative rates determined *via* k_2 and the branching ratios from eqn (7) are in excellent agreement with the values determined from the LIR and confirm the physical plausibility of the fitting parameters (Table 3). In addition, a clear trend in the RE–ligand distance dependence can be analyzed much more carefully given the higher precision of the nonradiative transition rates obtained from time-resolved spectroscopy. In fact, $k_{nr}(0)$ slightly increases from $YAl_3(BO_3)_4$:1% Eu^{3+} to $LuAl_3(BO_3)_4$:1% Eu^{3+} as expected according to the Ermolaev–Sveshnikova model[83] and in line with our earlier findings in β-$NaREF_4$:0.5% Eu^{3+} (RE = La, Y, Lu).[17] However, a slightly higher nonradiative rate persists in $GdAl_3(BO_3)_4$:1% Eu^{3+} than in $YAl_3(BO_3)_4$:1% Eu^{3+} despite a larger ionic radius of Gd^{3+} than Y^{3+} in sixfold coordination ($r(Gd^{3+})$ = 1.08 Å, $r(Y^{3+})$ = 1.04 Å)[84] analogously to the intrinsic nonradiative coupling strengths estimated from the temperature-dependent LIR (Fig. 6 and Table 3). Additional confirmation of the physical validity of this effect can be qualitatively assessed from the emission spectra depicted in Fig. 7. The relative intensity of the $^5D_1 \rightarrow {}^7F_2$ transition in $GdAl_3(BO_3)_4$:1% Eu^{3+} compared to that of the $^5D_0 \rightarrow {}^7F_2$ transition upon excitation into the $^5D_1$ level is indeed slightly smaller than in $YAl_3(BO_3)_4$:1% Eu^{3+} implying a slightly faster nonradiative decay responsible for the

Table 3 Measured decay rate of the $^5D_1$ level (k_2), branching ratios of the $^5D_1 \rightarrow {}^7F_2$ ($\beta_{1\to 2}$) and $^5D_0 \rightarrow {}^7F_2$ ($\beta_{0\to 2}$) according to eqn (8), the intrinsic nonradiative rate $k_{nr}(0)$ according to eqn (7) and $k_{nr}(0)$ obtained from the LIR, radiative rate of the $^5D_1$ level (k_{2r}) according to eqn (4) and (10) of $REAl_3(BO_3)_4$:1% Eu^{3+} (RE = Y, Gd, Lu)

Compound	k_2/ms^{-1}	$\beta_{1\to 2}$	$\beta_{0\to 2}$	$k_{nr}(0)$/ms^{-1}	$k_{nr}(0)$ (LIR)/ms^{-1}	k_{2r} from eqn (4)/ms^{-1}	k_{2r} from eqn (10)/ms^{-1}
$YAl_3(BO_3)_4$:1% Eu^{3+}	56.09 ± 0.01	0.2999	0.5990	55.16 ± 0.03	53 ± 8	0.93 ± 0.01	0.90 ± 0.05
$GdAl_3(BO_3)_4$:1% Eu^{3+}	57.18 ± 0.01	0.3220	0.6084	56.23 ± 0.04	54 ± 8	0.95 ± 0.01	0.98 ± 0.03
$LuAl_3(BO_3)_4$:1% Eu^{3+}	57.41 ± 0.01	0.3439	0.5962	56.47 ± 0.01	60 ± 5	0.94 ± 0.01	0.92 ± 0.04

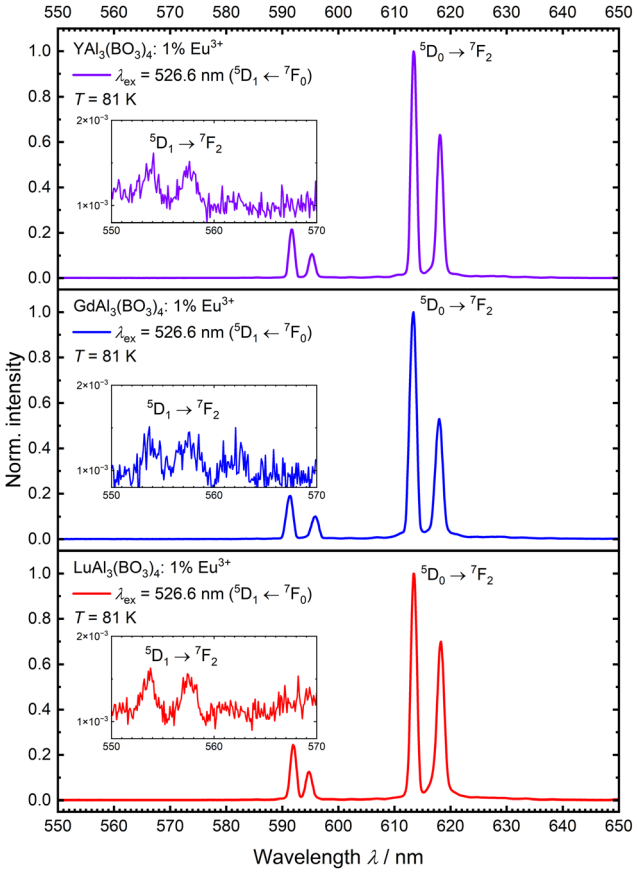

Fig. 7 Left: Normalized photoluminescence emission spectra of $REAl_3(BO_3)_4$:1% Eu^{3+} (RE = Y, Gd, Lu) upon excitation into the $^5D_1$ level at 81 K. The inset depicts the $^5D_1$-based emission.

observation of $^5D_0$-based emission in that experiment (Fig. 7). Consequently, it can be concluded that the nonradiative decay rate $k_{nr}(0)$ coupling the excited $^5D_1$ and $^5D_0$ levels of Eu^{3+} is indeed slightly larger in $GdAl_3(BO_3)_4$:1% Eu^{3+} than in $YAl_3(BO_3)_4$: 1% Eu^{3+} despite a shorter expectable average Eu–O bond length in the latter host compound. We ascribe this observation to the magnetic dipolar nature of the nonradiative $^5D_1 \leftrightarrow {}^5D_0$ transition and a local accelerating effect by the paramagnetic nature of neighboring Gd^{3+} ions. A very detailed investigation of this phenomenon on a wider scope of compounds is currently ongoing and will be part of a future study.

Besides the nonradiative decay from $^5D_1$ to $^5D_0$ level governed by multiphonon relaxation, radiative relaxation of the $^5D_1$ level remains to be discussed. By determining $k_{nr}(0)$ from eqn (5), the radiative rate k_{2r} can be simultaneously extracted by means of eqn (2). In all three Eu^{3+}-activated borates, it is in the order of 1 ms^{-1} (see Fig. 4) and thus, within the reported range for the $^5D_1$ level.[17,75,85] An alternative method to indirectly assess the radiative rate k_{2r} of the $^5D_1$ level is a complementary analysis of the $^5D_0$-related luminescence decay curves at elevated temperatures (Fig. 8). Over the entire temperature range, the decay curves can be fitted with a single-exponential model. The decay rates remain constant up to a temperature of just over 250 K, then show a gradual increase up to 700 K, and increase even more strongly above those temperatures. Over the entire temperature range, no structural phase transitions of the huntite-type borates $REAl_3(BO_3)_4$ (RE = Y, Gd, Lu) is observable,[86–88] which indicates that this temperature dependence must be a consequence of thermally activated processes. Multiphonon relaxation cannot be responsible for the observed temperature dependence of the decay rate of the $^5D_0$ already detectable above 400 K, given the very high energy gap to the lower $^7F_6$ level (around 12390 cm^{-1})[43] that would require at least 9 cut-off modes in the borate hosts (see Fig. 8). The slight increase in the decay rate of the $^5D_0$ level just above 250 K can be attributed to the onset of thermal coupling between the $^5D_1$ and $^5D_0$ levels, consistent with the observed minimum of the LIR at that temperature (Fig. 6) and the onset temperature (Table 3), above which the LIR follows Boltzmann behavior. In that temperature range, the $^5D_0$ and $^5D_1$ will decay with a thermally averaged decay rate $\langle k(T)\rangle$[89]

$$\langle k(T)\rangle = \frac{g_1 k_{1r} + g_2 k_{2r} \times \exp\left(-\frac{\Delta E}{k_B T}\right)}{g_1 + g_2 \times \exp\left(-\frac{\Delta E}{k_B T}\right)} \quad (9)$$

The stronger increase in the rate above 700 K is also in good agreement with the LIR, which no longer follows the usual course above 650 K (see Fig. 6). This may be related to the influence of the $Eu^{3+} \leftarrow O^{2-}$ LMCT state, which depopulates the $4f^6$ levels of Eu^{3+} *via* a thermally activated crossover and induces quenching.[82,90,91] Due to this process, eqn (9) is extended by a Mott–Seitz expression describing the crossover relaxation,[92] resulting in

$$K(T) = \langle k(T)\rangle + k_x(0) \times \exp\left(-\frac{\Delta E_x}{k_B T}\right) \quad (10)$$

with a connected intrinsic crossover rate $k_x(0)$ and ΔE_x as the effective barrier between the $^5D_0$ level and the crossing point with the potential energy curve of the LMCT state. The temperature-dependent decay rates of the $^5D_0$-based level can be fitted well by eqn (10) (Fig. 8). The fitted energy gaps between the $^5D_1$ and $^5D_0$ levels using eqn (10) are in the range of 1700 cm^{-1} and in excellent agreement with the spectrally determined energy gaps ($\approx$1750 cm^{-1}). In turn, the fitted crossover barrier ΔE_x (see Fig. 8 for exact value) is much below the anticipated value according to the excitation spectra of $REAl_3(BO_3)_4$:1% Eu^{3+} (RE = Y, Gd, Lu) (Fig. 3). However, as the crossover process only becomes relevant at very high temperatures (>700 K), only four independent data points can be effectively used to estimate the crossover rate $k_x(0)$ and barrier ΔE_x, which results in relatively large errors and thus, only offer limited insights. Higher temperatures could help make more precise statements and justify the validity of the model according to eqn (10) for the whole temperature range. By determining $k_{nr}(0)$ from eqn (7), the radiative rate k_{2r} can be obtained by rearranging eqn (4). This is in the range of about 1 ms^{-1} (Table 3) and generally matches the values estimated by eqn (10).

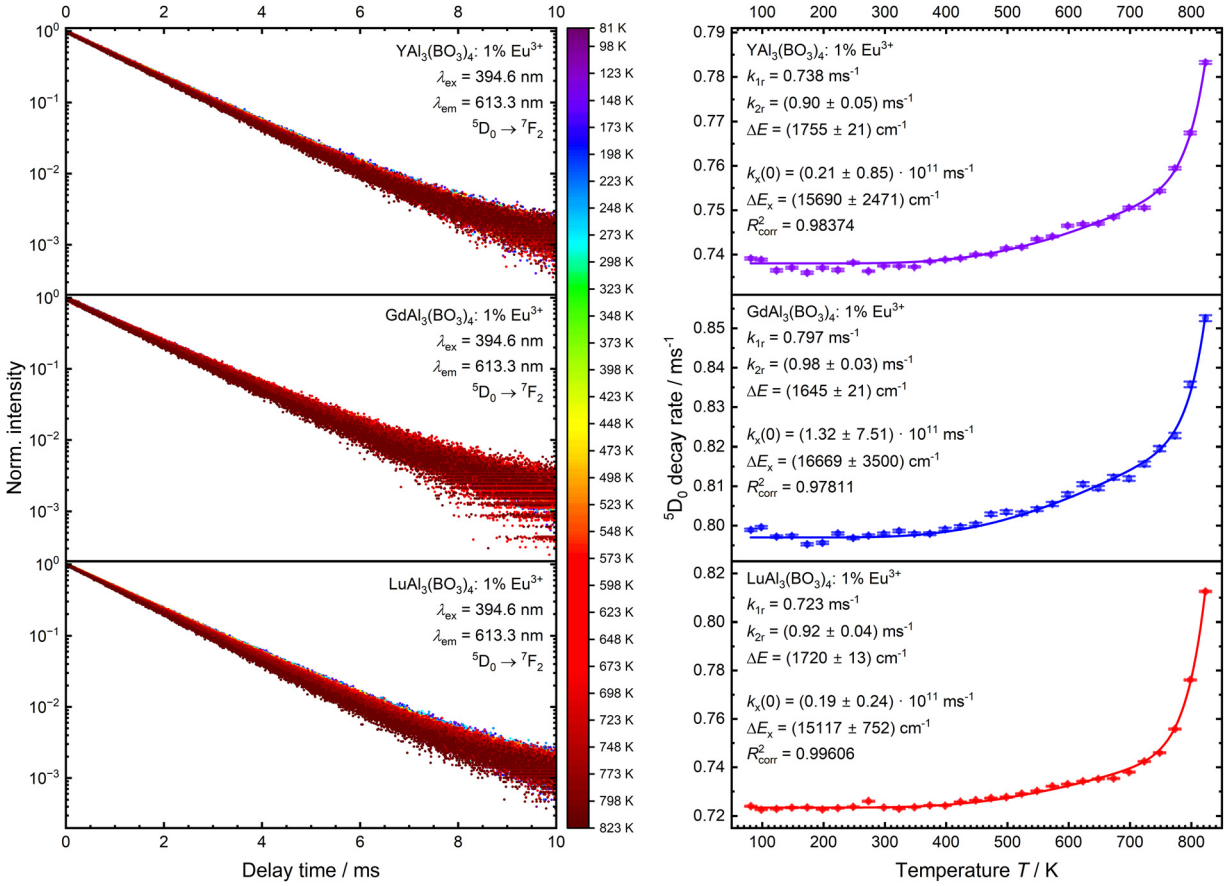

Fig. 8 Temperature-dependent decay curves of the $^5D_0$-based emission of $REAl_3(BO_3)_4$:1% Eu^{3+} (RE = Y, Gd, Lu) (left) and obtained decay rates as a function of temperature with a fit to eqn (10) (right).

Conclusions

In this work, the luminescent properties of Eu^{3+} in single-crystalline huntite-type $REAl_3(BO_3)_4$ (RE = Y, Gd, Lu) were investigated. Narrow-band emission in the red spectral range is observed, which can be attributed to emission from the $^5D_0$ level to the lower-energy ^7F_J (J = 0–4) levels. The splitting of the emission indicates a local D_3 symmetry of the $[REO_6]^{9-}$ coordination entities in $REAl_3(BO_3)_4$. The relative angular position of the six oxygen ligands correlates well with the trend in the decay times of the $^5D_0$ level, as well as the observed splitting of the $^5D_1$ or $^7F_1$ crystal field levels, respectively and with the different asymmetry ratio (R_2) values. In addition, weak narrow-band emission is observed in the green spectral range, which can be traced back to emission from the $^5D_1$ level. The comparatively weak emission from the $^5D_1$ level is in agreement with the energy gap law and the high cut-off phonon energy of $REAl_3(BO_3)_4$. The intrinsic nonradiative rate from the $^5D_1$ level into the $^5D_0$ level was determined both from the luminescence intensity ratio and time-resolved studies on the photoluminescence from the $^5D_1$ level. Both methods yield a rate in the range of $k_{nr}(0) \approx 55\ ms^{-1}$. The intrinsic nonradiative transition rate $k_{nr}(0)$ connecting the $^5D_1$ and $^5D_0$ level of Eu^{3+} tends to increase with decreasing average Eu–O bond length as could be demonstrated upon comparison between $YAl_3(BO_3)_4$:Eu^{3+} ($k_{nr}(0) = (55.16 \pm 0.03)\ ms^{-1}$) and $LuAl_3(BO_3)_4$:Eu^{3+} ($k_{nr}(0) = (56.47 \pm 0.01)\ ms^{-1}$). However, there is not the expected net decrease in the corresponding nonradiative transition rate in $GdAl_3(BO_3)_4$:Eu^{3+} ($k_{nr}(0) = (56.23 \pm 0.04)\ ms^{-1}$) compared to the Y congener, which we attribute to a local accelerating effect by the paramagnetic nature of neighboring Gd^{3+} ions. A very detailed investigation of this phenomenon on a wider scope of compounds is currently ongoing and will be part of a future study. The decay rate of the $^5D_0$ level shows a temperature dependence that reveals additional thermally activated processes. It is shown that the temperature dependence is due to the strong thermal coupling between the $^5D_0$ and $^5D_1$ levels, through which both decay with a thermally averaged rate, as well as crossover relaxation *via* the $Eu^{3+} \leftarrow O^{2-}$ ligand-to-metal charge transfer state. The models describing the temperature-dependent steady-state and time-resolved excited state dynamics demonstrated in this work thus offer the possibility of a detailed understanding of the excited state dynamics of the $^5D_1$ and $^5D_0$ levels of Eu^{3+} in $REAl_3(BO_3)_4$ (RE = Y, Gd, Lu). Nevertheless, further measurements should be carried out at higher temperatures to better understand and validate the models and, in particular, the relaxation process through the charge transfer state. Analysis of

other Eu^{3+}-activated host compounds at various temperatures also offers the possibility of verifying a more universal application of the presented model and can allow to assess the general applicability of Eu^{3+} as a targeted luminescent thermometer.

Conflicts of interest

There are no conflicts to declare.

Data availability

Source data generated in this study, which are presented in the main text and supplementary information (SI), are provided as a Source Data files *via* the Zenodo repository under the accession code https://doi.org/10.5281/zenodo.18346446. Source data is also available from the corresponding authors upon request. Supplementary information is available. See DOI: https://doi.org/10.1039/d5ma01480h.

Acknowledgements

M. S. gratefully acknowledges a scholarship of the ''Young College'' of the North-Rhine Westphalian Academy of Sciences, Humanities, and the Arts as well as funding by the Strategic Research Fund of the HHU Düsseldorf. The authors from the University of Verona (L. C., M. B., F. P.) thank the Facility ''Centro Piattaforme Tecnologiche'' (CPT) for access to the Rigaku SmartLab SE powder diffractometer.

References

1 D. Dutczak, T. Jüstel, C. Ronda and A. Meijerink, *Phys. Chem. Chem. Phys.*, 2015, **17**, 15236–15249.
2 M. Zhao, Y. Ge, Y. Li, X. Song, Z. Xia and X. Zhang, *Light: Sci. Appl.*, 2024, **13**, 266.
3 D. Dutzler, M. Seibald, D. Baumann and H. Huppertz, *Angew. Chem., Int. Ed.*, 2018, **57**, 13676–13680.
4 M. Zhao, H. Liao, M. S. Molokeev, Y. Zhou, Q. Zhang, Q. Liu and Z. Xia, *Light: Sci. Appl.*, 2019, **8**, 38.
5 P. Pust, V. Weiler, C. Hecht, A. Tucks, A. S. Wochnik, A. K. Henss, D. Wiechert, C. Scheu, P. J. Schmidt and W. Schnick, *Nat. Mater.*, 2014, **13**, 891–896.
6 G. J. Hoerder, M. Seibald, D. Baumann, T. Schroder, S. Peschke, P. C. Schmid, T. Tyborski, P. Pust, I. Stoll, M. Bergler, C. Patzig, S. Reissaus, M. Krause, L. Berthold, T. Hoche, D. Johrendt and H. Huppertz, *Nat. Commun.*, 2019, **10**, 1824.
7 M. Zhao, K. Cao, M. Liu, J. Zhang, R. Chen, Q. Zhang and Z. Xia, *Angew. Chem., Int. Ed.*, 2020, **59**, 12938–12943.
8 L. Zhang, J. Qiao, L. Wang, H. Guo, Q. Shi and Z. Xia, *Angew. Chem., Int. Ed.*, 2025, **137**, e202515249.
9 J. Qiao, D. Li, Q. Shi, H. Guo, P. Huang and L. Wang, *Light: Sci. Appl.*, 2024, **13**, 319.
10 A. Babu, F. Reveret, A. Barros, F. Cisnetti, K. Lemoine, D. Jamon, M. Suta, G. Chadeyron and D. Boyer, *ACS Appl. Mater. Interfaces*, 2025, **17**, 43413–43423.
11 T. A. Teichtmeister, T. Förster, A. H. Bernhart, M. Seibald, M. Suta and H. Huppertz, *Chem. Mater.*, 2024, **36**, 11462–11477.
12 L. Blois, I. F. Costa, J. Honorato, A. V. Sanches de Araújo, R. A. Ando, A. N. Carneiro Neto, M. Suta, O. L. Malta and H. F. Brito, *Inorg. Chem.*, 2024, **63**, 16861–16871.
13 J. Goldmann, T. Pier and T. Jüstel, *J. Lumin.*, 2025, **280**, 121091.
14 J. van Hest, G. A. Blab, H. C. Gerritsen, C. de Mello Donega and A. Meijerink, *J. Phys. Chem. C*, 2017, **121**, 19373–19382.
15 L. D. Carlos, R. A. Sá Ferreira, V. De Zea Bermudez, C. Molina, L. A. Bueno and S. J. L. Ribeiro, *Phys. Rev. B: Condens. Matter Mater. Phys.*, 1999, **60**, 10042–10053.
16 D. A. Turchetti, M. M. Nolasco, D. Szczerbowski, L. D. Carlos and L. C. Akcelrud, *Phys. Chem. Chem. Phys.*, 2015, **17**, 26238–26248.
17 T. P. van Swieten, J. M. Steenhoff, A. Vlasblom, R. de Berg, S. P. Mattern, F. T. Rabouw, M. Suta and A. Meijerink, *Light: Sci. Appl.*, 2022, **11**, 343.
18 N. Charczuk, S. Targońska, D. Zákutná, A. Watras, A. Patej and R. J. Wiglusz, *Ceram. Int.*, 2024, **50**, 14601–14613.
19 K. N. Kumar, L. Vijayalakshmi, P. K. Vishwakarma, K. Saijyothi, J. Lim and M. R. Siddiqui, *Mater. Charact.*, 2024, **213**, 114027.
20 C. Sun, G. Pratx, C. M. Carpenter, H. Liu, Z. Cheng, S. S. Gambhir and L. Xing, *Adv. Mater.*, 2011, **23**, H195–H199.
21 K. Singh, P. Pradhan, S. Priya, S. Mund and S. Vaidyanathan, *Dalton Trans.*, 2023, **52**, 13027–13057.
22 T. Pier and T. Jüstel, *Opt. Mater.: X*, 2024, **22**, 100299.
23 Y.-C. Lin, M. Karlsson and M. Bettinelli, in *Photoluminescent Materials and Electroluminescent Devices*, ed. N. Armaroli and H. J. Bolink, Springer International Publishing, Cham, 2017, pp. 309–355.
24 T. Pier and T. Jüstel, *Z. Kristallogr. – Cryst. Mater.*, 2025, **240**, 197–247.
25 P. A. Tanner, *Chem. Soc. Rev.*, 2013, **42**, 5090–5101.
26 P. Serna-Gallén, H. Beltrán-Mir and E. Cordoncillo, *Ceram. Int.*, 2023, **49**, 41078–41089.
27 K. Binnemans and C. Görller-Walrand, *J. Rare Earths*, 1996, **14**, 173–180.
28 K. Binnemans, *Coord. Chem. Rev.*, 2015, **295**, 1–45.
29 G. Jia, C. Wang and S. Xu, *J. Phys. Chem. C*, 2010, **114**, 17905–17913.
30 E. Zych, *J. Phys.: Condens. Matter*, 2002, **14**, 5637–5650.
31 J. A. Capobianco, P. P. Proulx, M. Bettinelli and F. Negrisolo, *Phys. Rev. B: Condens. Matter Mater. Phys.*, 1990, **42**, 5936–5944.
32 M. Bettinelli, A. Speghini, F. Piccinelli, A. N. C. Neto and O. L. Malta, *J. Lumin.*, 2011, **131**, 1026–1028.
33 S. Karaveli and R. Zia, *Opt. Lett.*, 2010, **35**, 3318–3320.
34 S. Karaveli and R. Zia, *Phys. Rev. Lett.*, 2011, **106**, 193004.
35 R. Brechbuhler, F. T. Rabouw, P. Rohner, B. le Feber, D. Poulikakos and D. J. Norris, *Phys. Rev. Lett.*, 2018, **121**, 113601.
36 Z. Wang, T. Senden and A. Meijerink, *J. Phys. Chem. Lett.*, 2017, **8**, 5689–5694.
37 K. H. Drexhage, *J. Lumin.*, 1970, **1–2**, 693–701.
38 R. D. Peacock, *Chem. Phys. Lett.*, 1975, **35**, 420–422.
39 B. R. Judd, *Phys. Rev.*, 1962, **127**, 750–761.
40 G. S. Ofelt, *J. Chem. Phys.*, 1962, **37**, 511–520.

41 F. T. Rabouw, P. T. Prins and D. J. Norris, *Nano Lett.*, 2016, **16**, 7254–7260.
42 W. Thor, A. N. Carneiro Neto, R. T. Moura, K.-L. Wong and P. A. Tanner, *Coord. Chem. Rev.*, 2024, **517**, 215927.
43 G. H. Dieke, H. M. Crosswhite and B. Dunn, *J. Opt. Soc. Am.*, 1961, **51**, 820–827.
44 V. Lojpur, S. Ćulubrk, M. Medić and M. Dramicanin, *J. Lumin.*, 2016, **170**, 467–471.
45 C. D. S. Brites, S. Balabhadra and L. D. Carlos, *Adv. Opt. Mater.*, 2018, **7**, 1801239.
46 M. Suta and A. Meijerink, *Adv. Theory Simul.*, 2020, **3**, 2000176.
47 P. Netzsch, M. Hämmer, E. Turgunbajew, T. P. van Swieten, A. Meijerink, H. A. Höppe and M. Suta, *Adv. Opt. Mater.*, 2022, **10**, 2200059.
48 A. Ćirić, S. Stojadinović and M. D. Dramićanin, *Opt. Mater.*, 2018, **85**, 261–266.
49 E. Cavalli, A. Speghini, M. Bettinelli, M. O. Ramírez, J. J. Romero, L. E. Bausá and J. García Solé, *J. Lumin.*, 2003, **102–103**, 216–219.
50 M. H. Bartl, K. Gatterer, E. Cavalli, A. Speghini and M. Bettinelli, *Spectrochim. Acta, Part A*, 2001, **57**, 1981–1990.
51 H. Y. P. Hong and K. Dwight, *Mater. Res. Bull.*, 1974, **9**, 1661–1665.
52 S. R. Chinn and H. Y. P. Hong, *Opt. Commun.*, 1975, **15**, 345–350.
53 A. Brenier and G. Boulon, *J. Lumin.*, 2000, **86**, 125–128.
54 M. O. Ramírez, L. E. Bausá, D. Jaque, E. Cavalli, A. Speghini and M. Bettinelli, *J. Phys.: Condens. Matter*, 2003, **15**, 7789–7801.
55 D. Jaque, J. Capmany, Z. D. Luo and J. G. Solé, *J. Phys.: Condens. Matter*, 1997, **9**, 9715–9729.
56 C. Görller-Walrand, P. Vandevelde, I. Hendrickx, P. Porcher, J. C. Krupa and G. S. D. King, *Inorg. Chim. Acta*, 1988, **143**, 259–270.
57 C. Görller-Walrand, E. Huygen, K. Binnemans and L. Fluyt, *J. Phys.: Condens. Matter*, 1994, **6**, 7797–7812.
58 F. Kellendonk and G. Blasse, *J. Chem. Phys.*, 1981, **75**, 561–571.
59 E. L. Belokoneva, A. V. Azizov, N. I. Leonyuk, M. A. Simonov and N. V. Belov, *J. Struct. Chem.*, 1981, **22**, 476–478.
60 S. Ruggieri, L. Ceccon, M. Bettinelli and F. Piccinelli, *ECS J. Solid State Sci. Technol.*, 2023, **12**, 066005.
61 L. Ceccon, S. Ruggieri, M. Bettinelli, I. R. Martin and F. Piccinelli, *Ceram. Int.*, 2025, **51**, 16471–16474.
62 L. Ceccon, S. Ruggieri, M. Bettinelli, L. D. Carlos, C. D. S. Brites, A. N. Carneiro Neto and F. Piccinelli, *Ceram. Int.*, 2025, **51**, 53426–53431.
63 H. Yilmaz, M. Isobe, O. Clemens, M. Suta and P. Puphal, *Opt. Mater.: X*, 2025, **25**, 100380.
64 G. R. Dillip, K. Mallikarjuna, S. J. Dhoble and B. D. P. Raju, *J. Phys. Chem. Solids*, 2014, **75**, 8–14.
65 V. Jubera, J. P. Chaminade, A. Garcia, F. Guillen and C. Fouassier, *J. Lumin.*, 2003, **101**, 1–10.
66 R. Sankar and G. V. Subba Rao, *J. Alloys Compd.*, 1998, **281**, 126–136.
67 L. Marciniak, Y. Guyot, D. Hreniak and W. Strek, *J. Lumin.*, 2016, **169**, 238–244.
68 Z. Tian, H. Liang, B. Han, Q. Su, Y. Tao, G. Zhang and Y. Fu, *J. Phys. Chem. C*, 2008, **112**, 12524–12529.
69 J. Sytsma, G. F. Imbusch and G. Blasse, *J. Chem. Phys.*, 1989, **91**, 1456–1461.
70 T. Förster, J. Reifenberger, T. Moumin, J. Helmbold, Z. Antic, M. D. Dramicanin and M. Suta, *Chem. Sci.*, 2025, **16**, 12309–12323.
71 R. G. Geitenbeek, H. W. de Wijn and A. Meijerink, *Phys. Rev. Appl.*, 2018, **10**, 064006.
72 L. A. Riseberg and H. W. Moos, *Phys. Rev. Lett.*, 1967, **19**, 1423–1426.
73 L. A. Riseberg and H. W. Moos, *Phys. Rev.*, 1968, **174**, 429–438.
74 P. Solarz and W. Ryba-Romanowski, *J. Phys. Chem. Solids*, 2003, **64**, 1289–1296.
75 M. Kaczkan, *Opt. Mater.*, 2016, **59**, 60–65.
76 D. Pi, F. Wang, X. Fan, M. Wang and Y. Zhang, *Spectrochim. Acta, Part A*, 2005, **61**, 2455–2459.
77 X. Zhang and H. J. Seo, *J. Alloys Compd.*, 2010, **503**, L14–L17.
78 Y. Ma, X. Zhou, J. Wu, Z. Dong, L. Cui, Y. Wang and A. Meijerink, *J. Am. Chem. Soc.*, 2025, **147**, 12925–12936.
79 J. Kappelhoff, B. Greve and T. Jüstel, *RSC Adv.*, 2024, **14**, 29992–29998.
80 M. de Jong, L. Seijo, A. Meijerink and F. T. Rabouw, *Phys. Chem. Chem. Phys.*, 2015, **17**, 16959–16969.
81 P. Dorenbos, *J. Mater. Chem. C*, 2023, **11**, 8129–8145.
82 W. H. Fonger and C. W. Struck, *J. Chem. Phys.*, 1970, **52**, 6364–6372.
83 V. L. Ermolaev and E. B. Sveshnikova, *J. Lumin.*, 1979, **20**, 387–395.
84 R. D. Shannon, *Acta Crystallogr., Sect. A*, 1976, **32**, 751–767.
85 W. Ryba-Romanowski, S. Gołvab, G. Dominiak-Dzik and P. Solarz, *Appl. Phys. A: Mater. Sci. Process.*, 2002, **74**, 581–586.
86 A. A. Prokhorov, L. F. Chernush, T. N. Melnik, R. Minikayev, A. Mazur, V. Babin, M. Nikl, J. Lancok and A. D. Prokhorov, *Sci. Rep.*, 2019, **9**, 12787.
87 E. Belokoneva, N. Leonyuk, A. Pashkova and T. Timchenko, *Kristallografiya*, 1988, **33**, 1287–1288.
88 E. V. Koporulina, N. I. Leonyuk, A. V. Mokhov and O. V. Pilipenko, *J. Solid State Chem.*, 2000, **154**, 317–320.
89 M. Suta, *Opt. Mater.: X*, 2022, **16**, 100195.
90 M. D. Chambers, P. A. Rousseve and D. R. Clarke, *J. Lumin.*, 2009, **129**, 263–269.
91 B. Tian, B. Chen, Y. Tian, X. Li, J. Zhang, J. Sun, H. Zhong, L. Cheng, S. Fu, H. Zhong, Y. Wang, X. Zhang, H. Xia and R. Hua, *J. Mater. Chem. C*, 2013, **1**, 2338–2344.
92 B. Bendel and M. Suta, *J. Mater. Chem. C*, 2022, **10**, 13805–13814.